Contents lists available at ScienceDirect

# Materials Today Communications

# Verification, validation, and parameter study of a computational model for corrosion pit growth adopting the level-set method. Part II: Stress corrosion

A. Fayezioghani [a],[*], R. Dekker [b], L.J. Sluys [a]

[a] Computational Mechanics Group, Department of 3MD, Faculty of Civil Engineering and Geosciences, DelftUniversity of Technology, Delft, the Netherlands
[b] Building Physics and Systems, TNO, Delft, the Netherlands

## ARTICLE INFO

## ABSTRACT

Structural components in corrosive environments such as pipelines, bridges, aircrafts, and turbines are imposed to stress corrosion. A stress corrosion model for pit growth should a) accurately consider the electrochemistry of the corrosion process, b) properly deal with the moving interface between solid and electrolyte, and c) effectively incorporates the synergism between corrosion and mechanical field at the interface. In Part II, the influence of mechanical loading is added to the approach described in Part I. Part II investigates the model's capabilities of simulating stress corrosion via a set of numerical examples of corrosion pitting which include experimental validation and uncertainty quantification of model parameters and properties.

## 1. Introduction

The first attempts to theorize the synergism between corrosion and mechanical stress may be traced back to the works of Scully [1–3]. Turnbull [4] gave a model of corrosion cracking assisted by environment which combined empirical models with mechanistic influences. Sieradzki and Newman [5] also proposed a model with the emphasis on transgranular crack propagation. Since stress corrosion is a multiscale (from atomic to millimeter scale) phenomenon, distinguishing the mechanisms of interaction between stress and corrosion [6] makes the modeling process much clearer. A common modeling approach of stress corrosion at microscale is direct consideration of influence of mechanical stresses on the rate of corrosion by Gutman's formula [7,8]. In this approach, the electrochemistry of the corrosion pit front is coupled with the change of surface energy density caused by the stresses. The approach adopted in this paper uses a simple one-way coupling of the corrosion rate to mechanical load.

Part II utilizes the same approach of the moving corrosion front (i.e. combining FEM with the level-set method) as in Part I. It also adds the important influence of the mechanical field of the solid domain on corrosion pit growth to the approach. Part II of this paper, similar to Part I, focuses on more extensively demonstrating capabilities of the model proposed by Dekker et al. [9] in simulating stress corrosion. First of all, sensitivity analyses of system response quantities (SRQs) of interest such as pit depth to finite element mesh size and nonlinear solution time step

size are performed for an example problem. Then, uncertainty quantification (UQ) of model parameters (e.g. the nonlocal length scale and the applied electric current) or model properties (e.g. the formula of scalar strain measure related to plasticity/ dislocation) or both is conducted. Experimental validation is included for those example problems for which experimental measurements are available.

## 2. Corrosion kinetics

Kinetics of corrosion is explained in Part I. Thus, this section deals with the influence of a mechanical field on corrosion.

### 2.1. Influence of electric overpotential on corrosion

The influence of electric overpotential can be incorporated in the electric current surface density as in the following equation

$$j_n = j_n^0 \gamma_{overpot} \tag{1}$$

where $j_n^0$ is the open-circuit (or exchange) electric current surface density which depends on the characteristics of the metal surface in interaction to the electrolyte and $\gamma_{overpot}$ is the overpotential multiplier which, for example, can be calculated by the Butler-Volmer equation [10]. However, in this paper, the overpotential-induced electric current surface density, $j_n^0 \gamma_{overpot}$, is directly applied to the specimen in the numerical

---

* Correspondence to: Faculty of Civil Engineering and Geosciences, Delft University of Technology, Stevinweg 1, 2628 CN Delft, the Netherlands.
*E-mail addresses:* a.fayezioghani@tudelft.nl (A. Fayezioghani), richard.dekker@tno.nl (R. Dekker), L.J.Sluijs@tudelft.nl (L.J. Sluys).

examples. Thus, the electric overpotential is not explicitly modeled.

## 2.2. Influence of mechanical load on corrosion

As pointed out in the introduction section, Gutman [7,8] proposed two contributing factors to the electric current surface density related to mechanical stresses: elastic stresses and plastic deformations. From thermodynamic laws, he concluded that only the part of the elastic deformation energy that changes material volume can contribute to the electric current surface density. This part is directly related to hydrostatic stresses and takes the following form as a modification multiplier to the electric current surface density

$$\gamma_{\text{elastic}} = \exp\left(\frac{|\sigma_{\text{h}}|V_{\text{M}}}{RT}\right) \tag{2}$$

where $\sigma_{\text{h}}$ is the hydrostatic stress, $V_{\text{M}}$ is the molar volume of metal, $R$ is the gas constant, $T$ is the absolute temperature, and $||$ is the absolute value operator. Furthermore, Gutman, based on the theory of elastic dislocations, proposed the contribution of plastic deformations to the electric current surface density as another multiplier

$$\gamma_{\text{plastic}} = \frac{e_{\text{eq}}}{\varepsilon_{\text{eq}}^0} + 1 \tag{3}$$

where $e_{\text{eq}}$ is a scalar strain measure related to plastic deformation and/or dislocations occurred in the material and $\varepsilon_{\text{eq}}^0$ is an equivalent elastic strain at the onset of the elastic-to-plastic change of material state. The overall influence of mechanical field is defined as

$$\gamma_{\text{mechanical}} = \gamma_{\text{elastic}} \, \gamma_{\text{plastic}} \tag{4}$$

where $\gamma_{\text{mechanical}}$ is the mechanical multiplier.

To consider the influence of the mechanical field on the corrosion, the mechanical multiplier (4) should be multiplied to equation (1):

$$j_{\text{n}} = j_{\text{n}}^0 \gamma_{\text{overpot}} \gamma_{\text{mechanical}}. \tag{5}$$

By using equation (5), we assume a one-way influence of mechanical field on corrosion.

## 3. Behavior of material under cyclic loads

This section presents the behavior of a solid material under cyclic loads according to the Chaboche model [11].

### 3.1. Material plasticity framework

It is assumed that the total strain is small and can additively be decomposed into elastic and plastic strain:

$$\boldsymbol{\varepsilon} = \boldsymbol{\varepsilon}^{\text{e}} + \boldsymbol{\varepsilon}^{\text{p}} \tag{6}$$

where $\boldsymbol{\varepsilon}$, $\boldsymbol{\varepsilon}^{\text{e}}$, and $\boldsymbol{\varepsilon}^{\text{p}}$ are the total, elastic, and plastic strain tensor, respectively. In addition, in this contribution, the hyperelasticity [12] and hyperplasticity framework [13] are utilized to model the mechanical behavior of the material. That is, a free energy potential scalar function is employed to derive mechanical and thermodynamic forces and a plastic flow potential scalar function is used to derive the rate of plastic strain and internal states:

$$\boldsymbol{\sigma}^{\text{T}} = \frac{\partial \Psi}{\partial \boldsymbol{\varepsilon}^{\text{e}}}, \quad \boldsymbol{\chi}^{\text{T}} = \frac{\partial \Psi}{\partial \boldsymbol{\beta}}, \quad R = \frac{\partial \Psi}{\partial \zeta} \tag{7}$$

and

$$\dot{\boldsymbol{\varepsilon}}^{\text{p}} = \lambda \frac{\partial \Upsilon}{\partial \boldsymbol{\sigma}^{\text{T}}}, \quad \boldsymbol{\beta} = -\lambda \frac{\partial \Upsilon}{\partial \boldsymbol{\chi}^{\text{T}}}, \quad \zeta = -\lambda \frac{\partial \Upsilon}{\partial R} \tag{8}$$

where $\Psi = \Psi(\varepsilon, \varepsilon^{\text{p}}, \boldsymbol{\beta}, \zeta)$ is the free energy potential, $\Upsilon = \Upsilon(\boldsymbol{\sigma}, \boldsymbol{\chi}, R, \boldsymbol{\varepsilon}^{\text{p}}, \boldsymbol{\beta}, \zeta)$ is the plastic flow potential, $\boldsymbol{\sigma}$ is the stress tensor, $\boldsymbol{\chi}$ is the internal force tensor, $R$ is the isotropic force scalar, $\beta$ is the internal deformation tensor, $\zeta$ is the isotropic deformation scalar, $\lambda$ is the plastic flow scalar, the superscript symbol T indicates the transpose operator, and the dot symbol over a quantity indicates the time derivative of that quantity. According to the conventional theory of plasticity, the growth of plasticity in the material occurs following the KKT[1] conditions

$$\dot{\lambda} \geq 0, \, f_{\text{y}} \leq 0, \, \lambda f_{\text{y}} = 0 \tag{9}$$

where $\dot{\lambda}$ is the plastic flow rate and $f_{\text{y}} = f_{\text{y}}(\boldsymbol{\sigma}, \boldsymbol{\chi}, R, \boldsymbol{\varepsilon}^{\text{p}}, \boldsymbol{\beta}, \zeta)$ is the yield scalar function.

### 3.2. Chaboche model

It is more convenient to explain the Armstrong-Frederick type plasticity model first since the Chaboche model is a generalization of this model in order to incorporate different mechanisms involved in cyclic plasticity. In the Armstrong-Frederick type plasticity model [14], the free energy and plastic flow potential function are

$$\Psi = \frac{1}{2}\boldsymbol{\varepsilon}^{\text{e}} : \boldsymbol{C} : \boldsymbol{\varepsilon}^{\text{e}} + \frac{1}{2}k_1\boldsymbol{\beta} : \boldsymbol{\beta} + W \tag{10}$$

and

$$\Upsilon = f_{\text{vM}} + \frac{1}{2}\frac{k_2}{k_1}\boldsymbol{\chi} : \boldsymbol{\chi} \tag{11}$$

where $\mathbf{C}$ is the fourth order tensor of Hooke's stiffness, $k_1$ and $k_2$ are the linear and nonlinear scalar kinematic hardening coefficients, respectively, $f_{\text{vM}}$ is the von Mises yield function (see A for details and formulation),

$$W = Q_\infty\left(\zeta + \frac{1}{b}(\exp(-b\zeta) - 1)\right) \tag{12}$$

is the isotropic free energy potential, $Q_\infty$ is the ultimate added stress of isotropic hardening, and $b$ is the exponential growth coefficient of the added stress of isotropic hardening. By substituting the specified equations of free energy and plastic flow potential (i.e. equations (10) and (11)) into equation (7), we obtain

$$\boldsymbol{\sigma} = \frac{1}{2}(\boldsymbol{C} : \boldsymbol{\varepsilon}^{\text{e}} + \boldsymbol{\varepsilon}^{\text{e}} : \boldsymbol{C}) \tag{13}$$

$$\boldsymbol{\chi} = k_1\boldsymbol{\beta} \tag{14}$$

$$R = Q_\infty(1 - \exp(-b\zeta)). \tag{15}$$

In addition, substituting equations (10) and (11) into equation (8) gives

$$\dot{\boldsymbol{\varepsilon}}^{\text{p}} = \dot{\lambda}\boldsymbol{N} \tag{16}$$

$$\dot{\boldsymbol{\beta}} = -\dot{\lambda}\boldsymbol{H} \tag{17}$$

$$\dot{\zeta} = -\dot{\lambda}B \tag{18}$$

where $\boldsymbol{N}$, $\boldsymbol{H}$, and $B$ are the plastic strain, the internal deformation, and the isotropic deformation flow direction, respectively (see A for details and formulation). Equations (13) to (18) hold for a 3D problem. It should be noted that a problem in a 1D or 2D spatial space is a special case of a 3D problem, which requires imposing special conditions on the problem formulation. For example, for a 2D plane strain or plane stress condition, the strains or stresses are required to be zero in the out-of-plane direction, which necessitates using the appropriate Hooke's

---

[1] Karush-Kuhn-Tucker

stiffness matrix for plane strain or stress condition $\widetilde{C}$ as well as substituting the modified total strain $\widetilde{\varepsilon}$ and modified plastic strain $\widetilde{\varepsilon^{\mathrm{p}}}$ for total and plastic strain, respectively:

$$\widetilde{\boldsymbol{\varepsilon}} = \boldsymbol{L}(\boldsymbol{\varepsilon}) \tag{19}$$

$$\widetilde{\boldsymbol{\varepsilon}^{\mathrm{p}}} = \boldsymbol{L}(\boldsymbol{\varepsilon}^{\mathrm{p}}) \tag{20}$$

where $\boldsymbol{L}$ is a linear transform function for the plane strain or stress condition such that

$$\boldsymbol{a} = \begin{pmatrix} a_{xx} & a_{xy} & a_{xz} \\ a_{yx} & a_{yy} & a_{yz} \\ a_{zx} & a_{zy} & a_{zz} \end{pmatrix} \overset{\boldsymbol{L}}{\mapsto} \widetilde{\boldsymbol{a}} = \begin{pmatrix} a_{xx} & a_{xy} & 0 \\ a_{yx} & a_{yy} & 0 \\ 0 & 0 & (a_{xx}+a_{yy})\varpi \end{pmatrix} \tag{21}$$

where **a** is a second order tensor in a 3D spatial space with orthogonal in-plane axes $x$ and $y$ and an out-of-plane axis $z$, $\varpi$ is a multiplier equal to 0 and $-\nu/(1-\nu)$ for a plane strain and plane stress condition, respectively, $\nu$ is the Poisson's ratio, and the tilde symbol $\sim$ over a quantity indicates that quantity is modified corresponding to plane strain or plane stress condition. These modifications are the reason why $\dot{\boldsymbol{\varepsilon}}^{\mathrm{p}}/\dot{\lambda}$ is not equal to **N** in general and must not be substituted for **N**, or the other way around, in the governing equations of plasticity.

Another point of attention is that the deviatoric part of the internal force and internal deformation tensors, in some publications, are used instead of these quantities themselves, or they are assumed to be deviatoric tensors. The deviatoricity of these quantities are mathematically assessed in B. A mathematical proof is also given in the appendix which shows that these quantities are deviatoric with the employed free energy and plastic flow potential in this paper. However, it is advised by the authors to use the internal force and internal deformation tensors (and not their deviators) in the governing equations because they may not be deviatoric for other problem conditions.

Chaboche model [11,15] incorporates different influencing mechanisms of cyclic plasticity by superposing different responses of internal forces into a single one:

$$\chi = \sum_m \chi^m \tag{22}$$

where $\chi^m$ is the internal force caused by the $m$th cyclic plasticity mechanism. In this work, the internal forces and internal deformations caused by different plasticity mechanisms are assumed to have the same mathematical form expressed by equations (14) and (17), respectively, but with different coefficients (i.e. different $k_1$ and $k_2$).

### 3.3. Calculation of quantities influencing corrosion

According to equation (5), two mechanical quantities influence the electric current surface density: the hydrostatic stress $\sigma_{\mathrm{h}}$ and the scalar strain measure related to plastic deformation and/or dislocation motion $e_{\mathrm{eq}}$. The hydrostatic stress is

$$\sigma_{\mathrm{h}} = \frac{1}{3}\sigma_{kk} \tag{23}$$

and two different definitions of the scalar plastic strain measure are used in this research. The first measure is the equivalent dislocation strain suggested by Dekker et al. [9]:

$$\dot{e}_{\mathrm{eq}} = \mathrm{sgn}(\chi : \dot{\boldsymbol{\varepsilon}}^{\mathrm{p}})\dot{\varepsilon}^{\mathrm{p}}_{\mathrm{eq}} \tag{24}$$

where sgn is the sign function:

$$\mathrm{sgn}(a) = \begin{cases} -1, & a < 0 \\ 0, & a = 0, \\ +1, & a > 0 \end{cases} \tag{25}$$

$\dot{\varepsilon}^{\mathrm{p}}_{\mathrm{eq}}$ is the equivalent plastic strain rate

$$\dot{\varepsilon}^{\mathrm{p}}_{\mathrm{eq}} = \sqrt{\frac{2}{3}\dot{\boldsymbol{\varepsilon}}^{\mathrm{p}} : \dot{\boldsymbol{\varepsilon}}^{\mathrm{p}}}, \tag{26}$$

and $e_{\mathrm{eq}} \geq 0$. This measure is useful when the cyclic load generates dislocation pile-ups that increase material resistance to corrosion. The second measure is proposed here as

$$e_{\mathrm{eq}} = \begin{cases} \varepsilon^{\mathrm{p}}_{\mathrm{eq}}, & \varepsilon^{\mathrm{p}}_{\mathrm{eq}} < e_{\mathrm{th},1} \\ e_{\mathrm{th},1}, & e_{\mathrm{th},1} \leq \varepsilon^{\mathrm{p}}_{\mathrm{eq}} \leq e_{\mathrm{th},2} \\ 0, & e_{\mathrm{th},2} < \varepsilon^{\mathrm{p}}_{\mathrm{eq}} \end{cases} \tag{27}$$

where $e_{\mathrm{th},1}$ and $e_{\mathrm{th},2}$ are parameters to be calibrated by experimental data. Equation (27) is applicable for both monotonic and cyclic loads by which dislocations are generated, dislocation pile-ups are formed, and finally dislocations move away from the corrosion surface. The equations (24) and (27) are used for cyclic and monotonic loads, respectively, in two different numerical examples in Section 4.

The physical tip of a corrosion crack, pit, or notch (either in its initiation or its growth period) is located on boundaries of finite elements, which means that the stresses and strains at the tip area are approximated indirectly from the nearest integration points. The drawback of this local calculation is that the tip experiences highly concentrated values and sharp changes from element to element, which is not observed in experiments. To mitigate this localization, a nonlocal approach of the mechanical field which influences the electric current surface density is proposed in [9] and is adopted in this paper. Thus, the local quantities in equations (23), (24), (26), and (27) are substituted by their nonlocal alternatives only for calculation of $\gamma_{\mathrm{elastic}}$ and $\gamma_{\mathrm{plastic}}$.

The nonlocal alternative of a local quantity $q$ is defined as

$$q^{\mathrm{nonloc}}(\boldsymbol{x}_{\mathrm{A}}) = \frac{\int_{\Omega} w(\boldsymbol{x}; \boldsymbol{x}_{\mathrm{A}}, \boldsymbol{\Lambda})\, q(\boldsymbol{x})\, \mathrm{d}\Omega}{\int_{\Omega} w(\boldsymbol{x}; \boldsymbol{x}_{\mathrm{A}}, \boldsymbol{\Lambda})\, \mathrm{d}\Omega} \tag{28}$$

where $\boldsymbol{x}_{\mathrm{A}}$ is the spatial position vector of point A, $\boldsymbol{x}$ is the spatial position vector of a point in the domain of integration, $\Omega$ is the whole spatial domain of problem, $w$ is the weight function, and $\boldsymbol{\Lambda}$ is the vector of parameters of the weight function. The weight function used in this contribution is

$$w(\boldsymbol{x}; \boldsymbol{x}_{\mathrm{A}}, \boldsymbol{\Lambda}) = \begin{cases} \gamma_{\mathrm{w}}^{\left(\frac{r}{l_{\mathrm{w}}}\right)^2}, & 0 \leq \frac{r}{l_{\mathrm{w}}} \leq 1 \\ 0, & 1 < \frac{r}{l_{\mathrm{w}}} \end{cases} \tag{29}$$

where $\mathrm{r} = \|\boldsymbol{x} - \boldsymbol{x}_{\mathrm{A}}\|$ is the Euclidean distance from point A, $\boldsymbol{\Lambda} = [\gamma_{\mathrm{w}}, l_{\mathrm{w}}]^{\mathrm{T}}$, $l_{\mathrm{w}}$ is the nonlocal length scale, and $\gamma_{\mathrm{w}}$ is the exponent basis which is chosen to be 0.001 for all numerical examples of Section 4.

## 4. Numerical examples

This section is designated for validation and uncertainty quantification of the stress corrosion model explained in the previous sections. A hybrid control scheme without passivation is adopted in the numerical examples. This scheme is defined by two rules: a) the activation control condition is imposed to all interface points at the start of simulation and to every interface point added (because of the interface motion) at the start of each time increment of the numerical solution and b) the diffusion control condition (or the activation control condition) is imposed to the interface points with concentrations equal to (or less than) the saturation concentration at each time increment of the numerical solution. It should be noted that the applied electric current surface density and the mechanical field do not influence the dissolution of metal ions in the diffusion control condition. Furthermore, in each numerical example, an overpotential-induced electric current surface density is applied and kept constant during the simulation (i.e. a
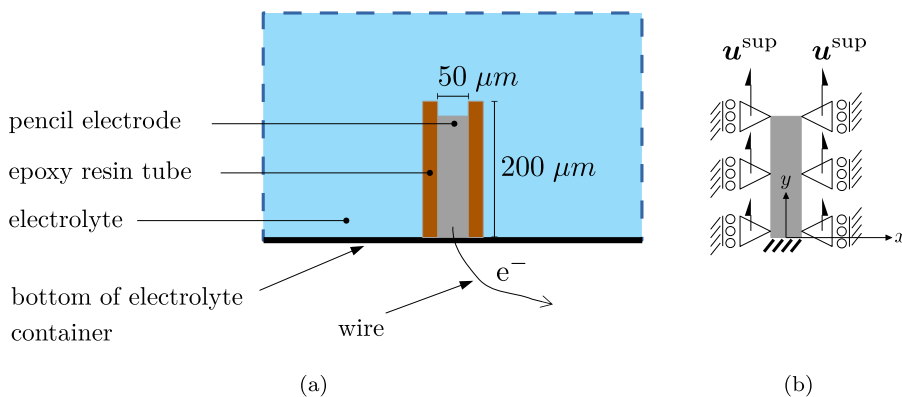
**Fig. 1.** The schematic view of the set-up of the pencil test with axial load example: (a) The specimen is a prismatic pencil electrode with a rectangular cross section. It is covered by an epoxy resin around its exterior surface in order to solely allow dissolution from its top. The electric current caused by the anodic dissolution flows out of the specimen via the wire at the bottom of the specimen. (b) The pencil specimen is fixed at the bottom, restrained in *x* direction on its exterior left and right surfaces, and free in the out-of-plane direction. The axial load is exerted by the support displacement $u^{\text{sup}}$ which is linearly increasing from $0\mu$ m at the bottom to $0.1\mu$ m at the top.

**Table 1**
Model parameters used in the pencil test with axial load example.

| | | | | | |
|---|---|---|---|---|---|
| $F$ | = | $96485.3\ \text{C} \cdot \text{mol}^{-1}$ | $E$ | = | $200 \times 10^3\ \text{MPa}$ |
| $R$ | = | $8.314\ \text{J} \cdot \text{mol}^{-1} \cdot \text{K}^{-1}$ | $\nu$ | = | $0.29$ |
| $z$ | = | $2.19$ | $\sigma_y$ | = | $117\ \text{MPa}$ |
| $c_S$ | = | $143.0 \times 10^{-6}\ \text{mol} \cdot \text{mm}^{-3}$ | $Q_\infty$ | = | $87\ \text{MPa}$ |
| $c_{\text{sat}}$ | = | $4.22 \times 10^{-6}\ \text{mol} \cdot \text{mm}^{-3}$ | $b$ | = | $9$ |
| $c_{\text{init}}$ | = | $0.0\ \text{mol} \cdot \text{mm}^{-3}$ | $k_1$ | = | $35.2 \times 10^3\ \text{MPa}$ |
| $D$ | = | $0.85 \times 10^{-3}\ \text{mm}^2 \cdot \text{s}^{-1}$ | $k_2$ | = | $300$ |
| $T$ | = | $293.15\ \text{K}$ | $l_w$ | = | $4\mu$ m |

galvanostatic condition for the applied electricity is assumed).

### 4.1. Example 1— Pencil test with axial load

In this numerical dissolution test, a steel electrode in an aqueous NaCl solution is subjected to axial loads exerted by displacements on its exterior surface. Figure 1 shows a schematic view of the test set-up and the dimensions of the specimen.

The pencil electrode is covered by an epoxy resin so that dissolution occurs only in the cross sectional area of the top of the electrode. The other end of the electrode is connected to a wire in order to conduct the electric current away from the corrosion interface and to measure the total electric current.

An initial depth of $21\mu$m is set, while $c = 0$ is assumed at the top of the computational electrolyte domain $\Gamma_{E,F}$. An overpotential-induced electric current surface density equal to $1.0$ mA/mm$^2$ is applied to the specimen. The specimen is modeled in a two-dimensional space with 3-noded triangular isoparametric finite elements subjected to the plane stress condition. Regarding the mechanical boundary conditions, the specimen is fixed at the bottom, and the exterior left and right surfaces of

the electrode are restrained by roller supports in *x* direction and are allowed to freely move in *y* direction. A linearly increasing displacement in *y* direction is imposed to the roller supports in order to model the axial load:

$$u^{\text{sup}} = \begin{bmatrix} 0 \\ 0.0005\ y \end{bmatrix} \qquad (30)$$

where $u^{\text{sup}}$ is the applied displacement. Additionally, the specimen is free in the out-of-plane direction. $\varepsilon_{\text{eq}}^{\text{p}}$ is used as the scalar plastic strain measure, and the evolution of the depth of the pencil electrode (i.e. the deepest point of the interface) in time is the SRQ of interest in this numerical example. The values of the model parameters are listed in Table 1.

Mesh and time step size sensitivity analyses of the model are carried out. Figure 2(a) shows the corrosion depth of the specimen in time for the time step size $\delta_{\text{time-step}} = 1.0$ s and for six mesh sizes $\delta_{\text{mesh}} \in \{0.5, 1.0, 2.0, 4.0, 6.0, 8.0\}\mu$ m. It is observed that the depth of the interface is insensitive to mesh sizes smaller than $2\mu$ m. To assess the time step size sensitivity, Figure 2(b) presents the corrosion depth for $\delta_{\text{mesh}} = 1.0\mu$ m and for three time step sizes $\delta_{\text{time-step}} \in \{0.1, 1.0, 4.2\}$ s. Figure 2(b) evidently depicts negligible sensitivity to the time step sizes. The depth is growing almost linearly (i.e. the interface velocity is almost constant) according to Figure 2. This is anticipated from the results of the model which uses a constant applied electric current surface density as well as the linear form of support displacements. It also expresses that the nonlocal length scale is large enough to overcome the discontinuities of stresses and strains caused by the finite element mesh type and size.

In order to better understand the motion of the corrosion front (i.e. the interface) and the influence of mechanical load on it, the contour map of metal ion concentration in the electrolyte domain and the mechanical multiplier in the solid domain are illustrated in Figure 3. It is
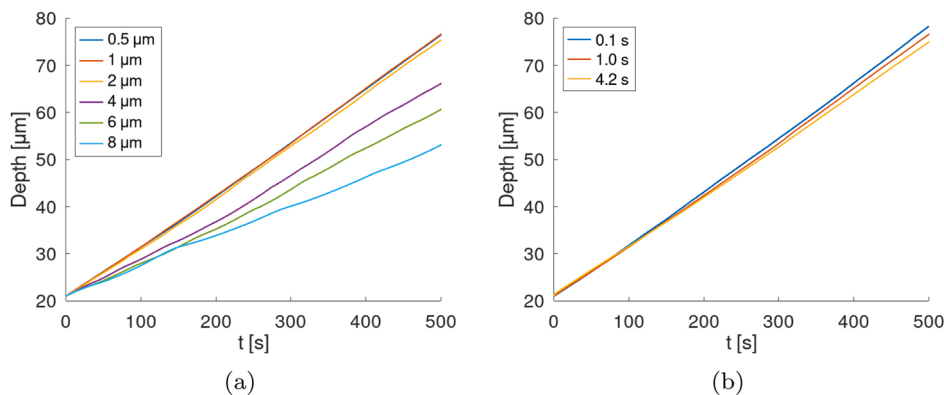


**Fig. 2.** Mesh and time step size sensitivity analysis of the depth evolution in the pencil test with axial load example: (a) the depths converge to a certain value as the mesh sizes decrease to below $2\mu$ m. (b) the depth of specimen in time shows negligible sensitivity to the time step sizes.
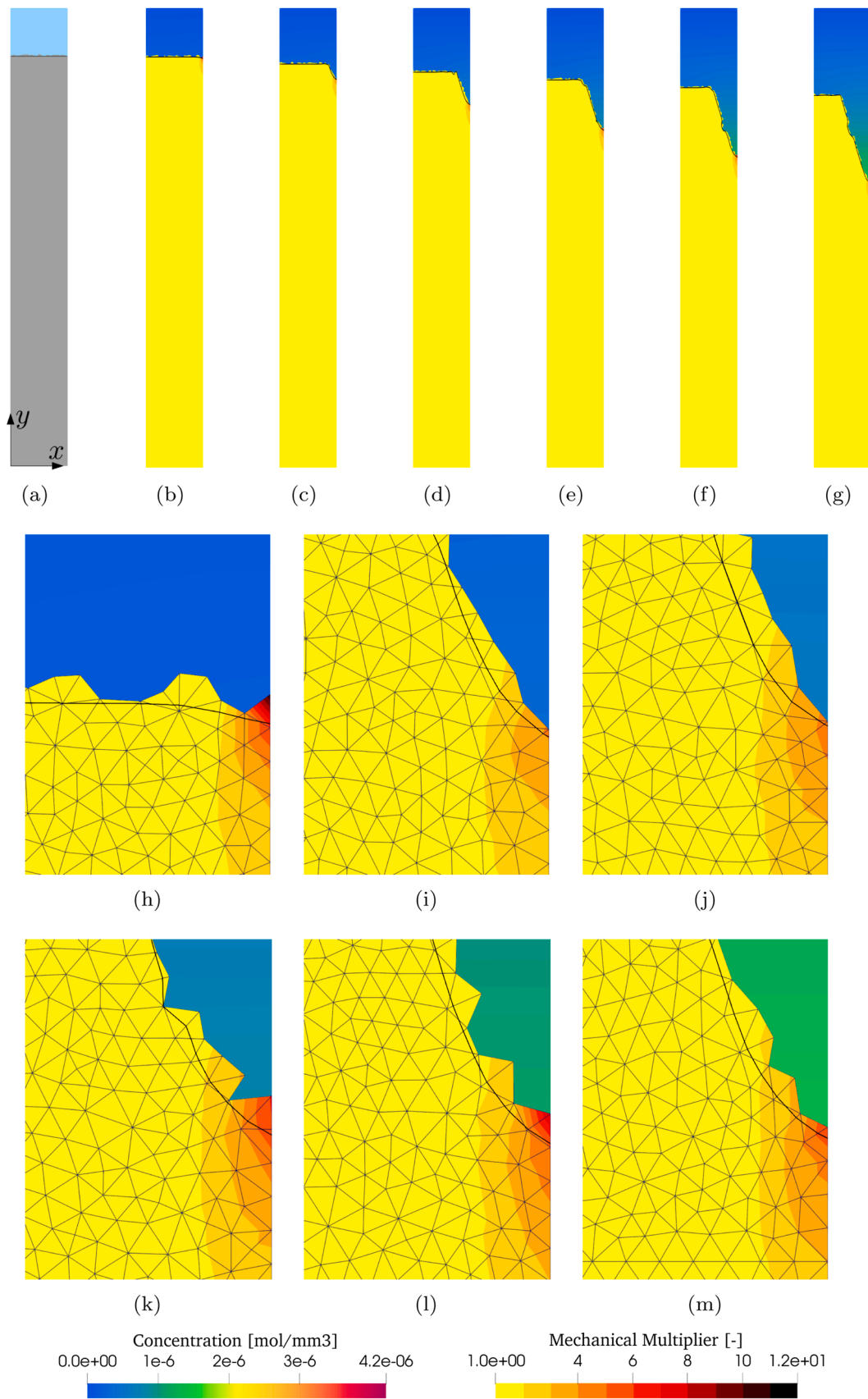
**Fig. 3.** The pencil test with axial load at the initial configuration in the subfigure (a), at times $t = 10, 100, 200, 300, 400, 500$ s in the subfigures (b) to (g), and their zoomed-in views in the subfigures (h) to (m), respectively. The contour maps of the local value of the metal ion concentration $c$ and the mechanical multiplier $\gamma_{\text{mechanical}}$ are shown in the electrolyte and solid domain, respectively. The solid bold black line indicates the interface. Because of symmetry of the problem with respect to $y$ axis, only the right half of the specimen is shown.
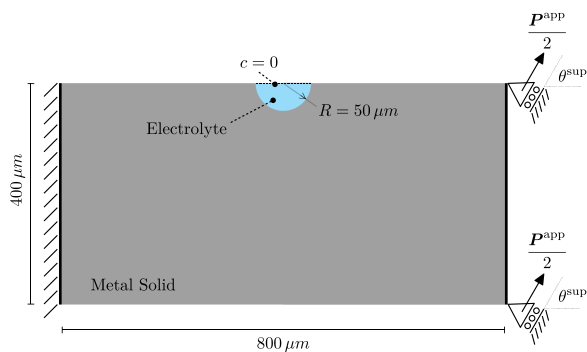
**Fig. 4.** The schematic view of the two-dimensional pit growth test with mechanical load. The initial semi-circular corrosion pit is located in the middle top of the metal solid specimen. The solid domain is fixed at its left edge and can freely move by a rigid body displacement in an angle of $\theta^{\mathrm{sup}}$ at its right edge. The force $\boldsymbol{P}^{\mathrm{app}}$ is applied in the direction with an angle of $\theta^{\mathrm{sup}}$, too.
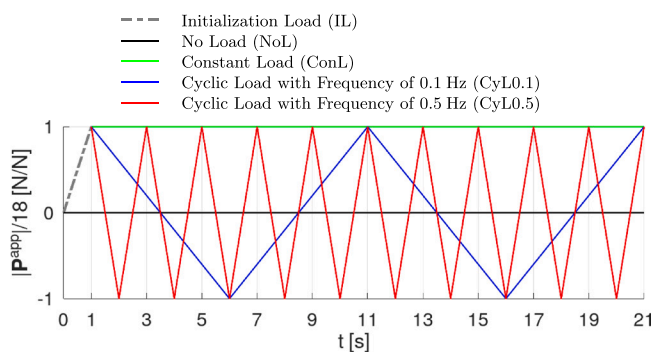


**Fig. 5.** The loads applied in the two-dimensional pit test with mechanical load. In order to start the loading of specimen from zero, the 'Initialization Load' applies to constant and cyclic loads.

observed in the figure that a) the interface motion is faster in the area close to the loading surface of the specimen (i.e. the area with large mechanical multiplier), b) the size of the region with high mechanical multiplier is small in comparison to the whole specimen size, c) the size of the flat surface on the top middle of the specimen is reducing in time due to the faster progressing front caused by the localized mechanical multiplier at the loading surfaces of the specimen, and d) discontinuities in the local mechanical multiplier exist because of the nonuniform mesh configuration but can be overcome by the nonlocal quantities. It should be noticed that the contour maps of the figure show local values, but the corrosion rate and consequently the interface motion are intensified based on the nonlocal values of the hydrostatic stress and the scalar plastic strain measure on the interface surface as described in Section 3.3.

### 4.2. Example 2— Two-dimensional corrosion pit growth test with mechanical load

This example, like the pencil test with axial load, is designed to simulate the dissolution of metal into an aqueous NaCl solution in a two-dimensional corrosion pit subjected to mechanical loads. See Figure 4 for a schematic illustration of the specimen.

An initial semi-circular corrosion pit with a radius of $50\mu$ m is located at the top center of the solid specimen. The boundary condition on top of the pit is assumed to be $c = 0$. Two-dimensional 4-noded rectangular isoparametric finite elements are used together with a plane stress condition. The specimen is fixed at its left edge while the right edge can rigidly move by means of roller supports under an angle $\theta^{\mathrm{sup}} = 80^{\circ}$. The applied load $\boldsymbol{P}^{\mathrm{app}}$ with magnitude 18 N is exerted on the right edge in the

same direction as the roller supports. Because of applying cyclic loads to the specimen, equation (24) is used to calculate the scalar plastic strain measure $e_{\mathrm{eq}}$. It is worth noting that this $e_{\mathrm{eq}}$ will automatically be equal to $\varepsilon_{\mathrm{eq}}^{\mathrm{p}}$ in case of constant loads. The SRQ of interest is chosen to be the topology evolution of the interface. The focus is on the notch which grows at the interface area where high values of the mechanical multiplier occur during the simulations. The values of all parameters are the same as those in Table 1 except $D = 0.575 \times 10^{-3}$ mm$^2 \cdot$ s$^{-1}$, $T = 288.15$ K, and $k_1 = 52.8 \times 10^3$ MPa.

The influence of three parameters: a) the nonlocal length scale $l_{\mathrm{w}}$, b) the overpotential-induced electric current surface density $j_{\mathrm{n}}^0 \gamma_{\mathrm{overpot}}$, and c) the applied load is assessed in the simulations. The applied loads are explained in Figure 5.

The first set of simulations is performed with $j_{\mathrm{n}}^0 \gamma_{\mathrm{overpot}} = 1.0$ mA/ mm$^2$, $l_{\mathrm{w}} = 4\mu$ m, and all of the applied load types. Figure 6 illustrates the contour maps of metal ion concentration and mechanical multiplier in the electrolyte and solid domain, respectively. It also visually presents a comparison of the interface and notch evolution of the specimen for different load types. The notch initiates from the bottom-right region of the interface where the mechanical multiplier is localized. At $t = 39$ s, the notch in CyL0.5 has started to rapidly grow, but the notches in the other two load types are almost the same. $t = 96$ s is the time when the deepest point of the notch reaches diffusion control in CyL0.5. Around $t = 122$ s, the interface in ConL starts to grow neighboring notches (say, left and right notch). This occurs because two points on the interface will have almost the same highest mechanical multiplier. At $t = 149$ s, the left notch in ConL is deeper than the right notch although its mechanical multiplier is smaller. In addition, the notch in CyL0.5 is shaped like a plate because of the diffusion control condition. At $t = 186$ s, the notch in CyL0.1 is close to reaching the diffusion control condition where the notch in CyL0.5 is mostly growing in the regions with activation control. Additionally, the left notch of ConL is growing deeper than CyL0.1. In summary, a) notch growth occurs in a localized region of the interface in comparison to the interface size, b) ConL, in a short time interval after the start of the test, has mechanically influenced a larger but less localized region of the interface than CyL0.1, c) ConL has started to grow neighboring notches one of which finally becomes dominant, and d) the mechanical multiplier magnitude and localization of CyL0.5 is higher than those for the other load types, which causes both a sharp and fast notch growth and a fast switching to the diffusion control condition that finally slows down the fast growth of the corrosion front.

The second set of simulations is designed to quantify the uncertainty in the nonlocal length scale. The simulations are done for $l_{\mathrm{w}} \in \{4, 8, 12\}\mu$ m, $j_{\mathrm{n}}^0 \gamma_{\mathrm{overpot}} = 1.0$ mA/ mm$^2$, and all of the applied load types. The evolution of the interface is presented in Figure 7. The evolution of the interface in these figures demonstrates that a) the notch starts from almost the same location for all $l_{\mathrm{w}}$, b) a larger $l_{\mathrm{w}}$ makes the notch shape more blunt and the notch growth slower, c) a larger $l_{\mathrm{w}}$ causes a later switch to diffusion control at the bottom of the notch, and d) unlike using $l_{\mathrm{w}} = 4\mu$ m which forms two notches in ConL, using $l_{\mathrm{w}} = 8$ or $12\mu$ m yields only one notch because of a more uniform distribution of the mechanical multiplier on the interface surface.

The last set of simulations of this numerical example assesses the influence of electric current surface density on the notch topology. Figure 8 draws the interface and notch for $l_{\mathrm{w}} = 4\mu$ m, $j_{\mathrm{n}}^0 \gamma_{\mathrm{overpot}} \in \{0.5, 1.0\}$ mA/ mm$^2$, and all of the applied load types. It can be observed from the figure that a) the depth of the notch is not linearly dependent on the electric current surface density, b) a smaller electric current surface density postpones the switch to diffusion control at the bottom of the notch, and c) the two notch in ConL form for all values of the electric current surface density.
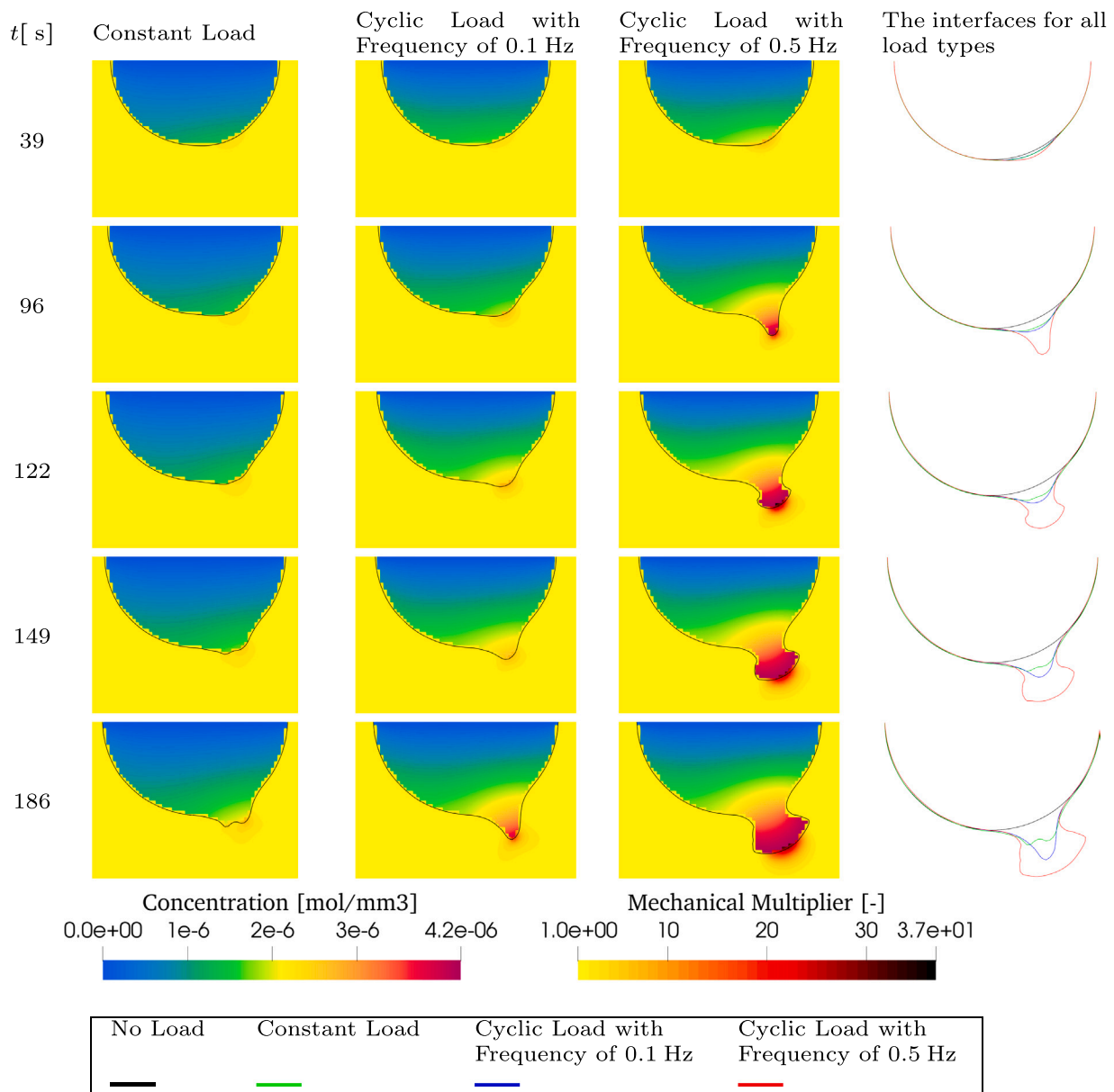
| $t[\,s]$ | Constant Load | Cyclic Load with Frequency of 0.1 Hz | Cyclic Load with Frequency of 0.5 Hz | The interfaces for all load types |

**Concentration [mol/mm3]**
0.0e+00   1e-6   2e-6   3e-6   4.2e-06

**Mechanical Multiplier [-]**
1.0e+00   10   20   30   3.7e+01

| No Load | Constant Load | Cyclic Load with Frequency of 0.1 Hz | Cyclic Load with Frequency of 0.5 Hz |

**Fig. 6.** Zoomed views of the corrosion pit and the notch at its bottom in the two-dimensional corrosion pit growth test with mechanical load example for different load types at selected times. Contour maps of the metal ion concentration and the local mechanical multiplier are illustrated in the electrolyte and solid domain, respectively. The solid bold black line indicates the interface in the contour maps. The notch initiates from the bottom-right region of the interface and grows faster as time proceeds.

### 4.3. Example 3— C-ring test

The C-ring test is a test provided by the Chinese standard GB/T 15970.5–1998 for stress corrosion of metals and alloys [16]. See Figure 9(a) for the geometry and dimensions of the specimen. Dai et al. [16] have experimentally investigated stress corrosion of Q345R steel by this test and have reported pit/crack length evolution which is utilized for calibration and validation in this numerical example. In the test, a constant displacement is exerted to the specimen by a bolt passed through the 6 mm-diameter hole, and the specimen is immersed into hydrofluoric acid. The experimental results by Dai et al. [16] show that the free corrosion weight loss of the specimen is almost constant, which is an appropriate characteristic for the assumption of constant overpotential-induced electric current surface density in this paper.

An initial semi-circular pit on top of the ring with a radius of approximately $7.0\mu$ m is assumed where $c = 0$ at its top surface. A finite element model is used with two-dimensional 4-noded rectangular

isoparametric finite elements under the plane stress condition. The specimen is hinged at its left and is roller at its right where it is allowed to freely move in $x$ direction (see Figure 9(b)). A constant displacement in $x$ direction, $u^{\text{sup}}$, is imposed to the roller support in order for the initial maximum circumferential stress $\sigma_t$ to be $0.55\sigma_y$ and $0.80\sigma_y$ in two separate experiments in correspondence to [16]. Based on the experimental observations of [16], the scalar plastic strain measure $e_{\text{eq}}$ is proposed here to take the form of equation (27). Additionally, the overpotential-induced electric current surface density is set approximately equal to 0.23 mA/ mm$^2$ in accordance with the average free corrosion in the first four hours of the experiment. A power law constitutive model is used for the material behavior of the steel according to Cui et al. [17]. Although the power law material model is a plasticity model used for monotonic (and not cyclic) loads, it is implemented with two minimal changes in the Chaboche model: a) assuming $k_1 = 0$ implies $\chi = 0$ which means no cyclic behavior mechanism is involved and b) using the following equation for the isotropic free
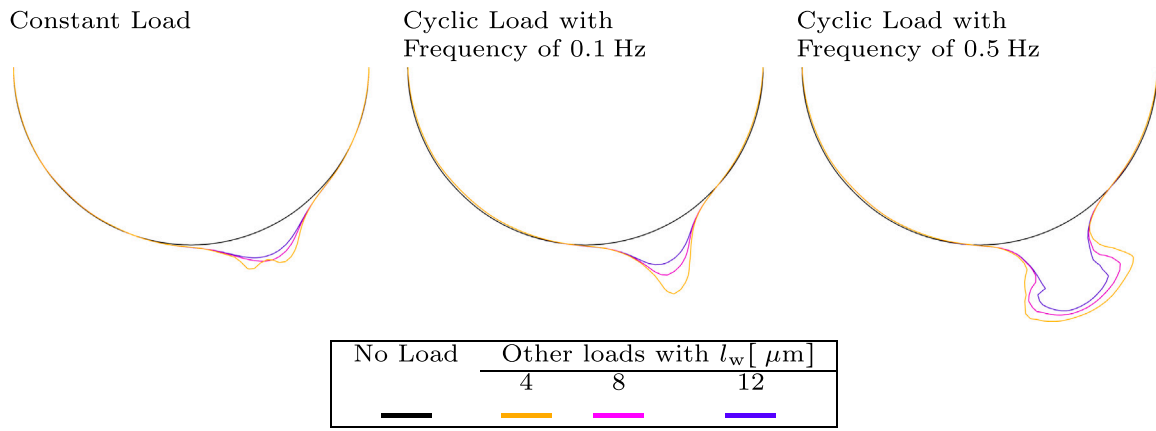
Constant Load　　　Cyclic Load with Frequency of 0.1 Hz　　　Cyclic Load with Frequency of 0.5 Hz

| No Load | Other loads with $l_w [\mu m]$ | | |
|---------|:---:|:---:|:---:|
|         | 4 | 8 | 12 |

**Fig. 7.** Zoomed views of the interface in the two-dimensional corrosion pit growth test with mechanical load example for different load types and nonlocal length scales at $t = 186$ s. As expected, the smaller the nonlocal length scale, the faster the notch grows.
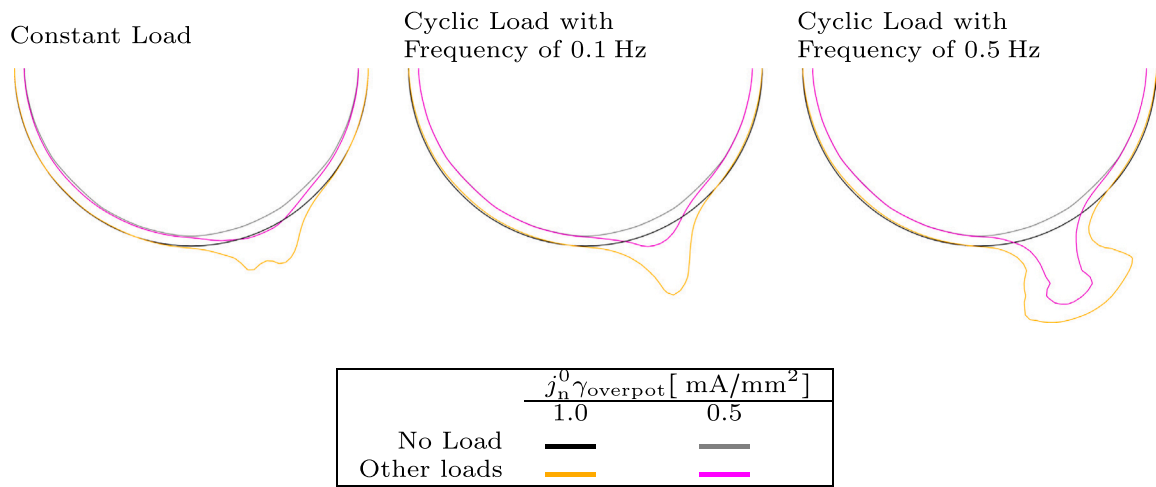
Constant Load　　　Cyclic Load with Frequency of 0.1 Hz　　　Cyclic Load with Frequency of 0.5 Hz

| | $j_n^0 \gamma_{overpot} [\text{mA/mm}^2]$ | |
|---|:---:|:---:|
| | 1.0 | 0.5 |
| No Load | | |
| Other loads | | |

**Fig. 8.** Zoomed views of the interface in the two-dimensional corrosion pit growth test with mechanical load example for different load types and overpotential-induced electric current surface densities at $t = 186$ s. As expected, the larger the electric current surface density, the faster the notch grows.
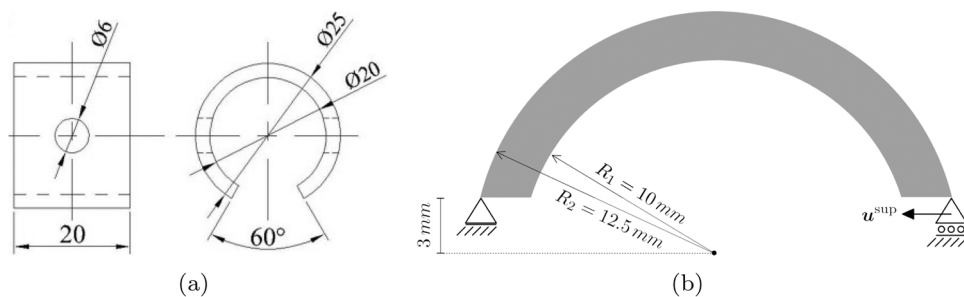
**Fig. 9.** The C-Ring test set-up: a) geometry and dimensions in mm [16] and b) computational geometry and boundary conditions.

energy potential

$$W = \sigma_y \left( \frac{\varepsilon_{eq}^0}{N+1} \left( \left( 1 + \frac{\zeta}{\varepsilon_{eq}^0} \right)^{N+1} - 1 \right) - \zeta \right) \tag{31}$$

where $N$ is a parameter which can be calibrated from the data of a tensile test and $\varepsilon_{eq}^0$ is assumed to be equal to $\sigma_y/E$. Here, the SRQ of interest is the depth of the corrosion pit. The parameters of the model are the same as in Table 1 except $c_{sat} = 5.1 \times 10^{-6}$ mol/ mm$^3$, $\nu = 0.25$, $\sigma_y = 535$ MPa, $N = 0.073$, and $l_w = 50\mu$ m.

The length of the pit reported in [16] is defined as the vertical difference between the deepest point of the pit and the initial non-corroded surface. Therefore, the pit length can be divided into two lengths: the vertical difference a) between the deepest point and top of the pit, called 'pit depth', and b) between the top of the pit and the initial noncorroded surface, called 'surrounding corrosion length'. According to the experimental observations in [16], the surrounding corrosion length grows faster than the pit depth in a time interval from the start of each experiment, called 'time interval I'. This interval is followed by an interval in which the growth speed of the two lengths are comparable, called 'time interval II'. Afterwards, the pit develops much faster than the surrounding corrosion, called 'time interval III'. Based on finite
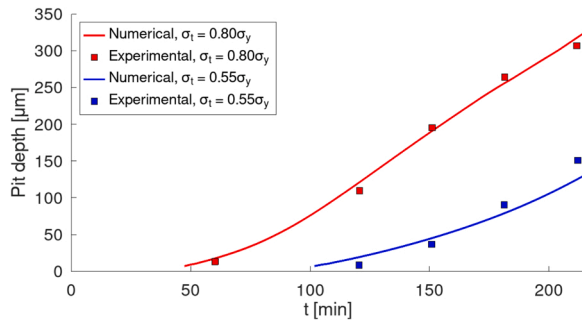
**Fig. 10.** The pit depth evolution in the C-ring test example. The numerical depths show good accordance to experimental data. Note that the numerical curves start from the time interval II.

element simulations of the C-ring, the speed of the surrounding corrosion is assumed to be constant and spatially uniform on a large surface (in comparison to the pit size) of the specimen around the pit. Thus, only pit growth in the time interval II and III are simulated and assessed.

The pit depth is plotted versus time for the two loading cases in Figure 10. As pointed out above, the constant surrounding corrosion speed is assumed to be 0.450 and 0.238$\mu$ m/ min for $\sigma_t = 0.80\sigma_y$ and 0.55$\sigma_y$, respectively. Furthermore, the nonlocal length scale as well as parameters for the scalar plastic strain measure are calibrated based on the experimental results related to $\sigma_t = 0.80\sigma_y$: $e_{th,1} = 0.0035$ and $e_{th,2} = 0.0280$. Then, they are validated for the experimental results related to $\sigma_t = 0.55\sigma_y$. The figure shows that the simulations are in good accordance with the experimental data. In addition, the numerical results depict that the proposed strain measure can appropriately be employed to model the accelerating and decelerating experimental pit depth growths.

## 5. Conclusions

Numerical examples have been designed in Part II to demonstrate the performance of the stress corrosion model developed in [9]. Overall, it can be concluded from the numerical results that a) the stress corrosion model is not sensitive to mesh and time step size for the simulated cases, b) the employed nonlocal formulation has successfully overcome local discontinuities caused by mesh type and size, c) there is uncertainty in the nonlocal length scale which should be quantified, where the results can be compared to experimental data, and d) the scalar plastic strain measure should include the influence of plastic deformations and/or dislocations on the activation energy of corrosion for the problems under investigation. Regarding the simulation results of the pencil test with

axial load, the model gives a linear depth evolution which is anticipated from the governing equations and its linear loading. The simulation results of the two-dimensional pit test with mechanical load emphasizes the significance of selecting a proper value for the nonlocal length scale. It also shows a nonlinear interface evolution with respect to the applied electric current. From the C-ring test simulation results, it is observed that the proposed scalar plastic strain measure is successful in de/intensifying the pit depth in order to fit numerical results to experimental data.

It is finally noted that localized corrosion may be caused by material dissolution assisted by mechanical field and by the rupture of a passivated film on the interface [18]. A model which includes the first component is assessed in this paper. However, the second component is not covered here but can be incorporated in the current stress corrosion model by introducing interface elements at the common surface between each solid and electrolyte element. By using the interface elements, it will be possible a) to model the electrochemical behavior of the film and b) to model plasticity of the film and to calculate the mechanical history (e.g. stress and strain) of the film. The interface elements condense the electromechanochemical mechanisms related to the interface (e.g. passivation process and the film rupture).

## Declaration of Competing Interest

The authors declare that they have no known competing financial interests or personal relationships that could have appeared to influence the work reported in this paper

## Data Availability

Data will be made available on request.

*CRediT authorship contribution statement*

**A. Fayezioghani:** Conceptualization, Methodology, Software, Formal analysis, Writing – original draft, Writing – review & editing. **R. Dekker:** Methodology, Software, Writing – review & editing. **L. J. Sluys:** Conceptualization, Supervision, Funding acquisition, Writing – review & editing.

## Appendix A. von Mises yield function, plastic strain, and internal states

The von Mises yield function is

$$f_{vM} = \sqrt{3J_2(\boldsymbol{\alpha})} - \kappa \tag{A.1}$$

where

$$\boldsymbol{\alpha} = \boldsymbol{\sigma} - \boldsymbol{\chi} \tag{A.2}$$

is the overstress tensor,

$$\kappa = \sigma_y + R \tag{A.3}$$

is the total isotropic stress, $\sigma_y$ is the yield stress of virgin material,

$$J_2(\boldsymbol{a}) = \frac{1}{2}\boldsymbol{a}^{Dev} : \boldsymbol{a}^{Dev} \tag{A.4}$$

is the second invariant of the deviator of tensor $\boldsymbol{a}$, $\boldsymbol{a}^{\text{Dev}}$ is the deviatoric part of (or the deviator of) the second order tensor $\boldsymbol{a}$:

$$\boldsymbol{a}^{\text{Dev}} = \boldsymbol{a} - \boldsymbol{a}^{\text{Hyd}}, \tag{A.5}$$

$\mathbf{a}^{\text{Hyd}}$ is the hydrostatic part of the second order tensor $\mathbf{a}$:

$$a_{ij}^{\text{Hyd}} = \frac{1}{3}a_{kk}\delta_{ij}, \tag{A.6}$$

$\delta_{ij}$ is the Kronecker delta:

$$\delta_{ij} = \begin{Bmatrix} 1, & i = j \\ 0, & i \neq j \end{Bmatrix}, \tag{A.7}$$

and : is the double-dot operator between two $n$th order tensors $\mathbf{b}$ and $\mathbf{c}$ such that

$$\boldsymbol{b} : \boldsymbol{c} = \boldsymbol{b}_{\ldots kl}c_{lk\ldots}. \tag{A.8}$$

Considering the von Mises function (A.1) as the yield function and substituting equations (10) and (11) into equation (8) gives the following flow directions for the employed Chaboche model

$$N = \sqrt{\frac{3}{2}} \frac{\boldsymbol{\alpha}^{\text{Dev}}}{\sqrt{\boldsymbol{\alpha}^{\text{Dev}} : \boldsymbol{\alpha}^{\text{Dev}}}}, \tag{A.9}$$

$$H = -\sqrt{\frac{3}{2}} \frac{\boldsymbol{\alpha}^{\text{Dev}}}{\sqrt{\boldsymbol{\alpha}^{\text{Dev}} : \boldsymbol{\alpha}^{\text{Dev}}}} + \frac{k_2}{k_1}\boldsymbol{\chi}, \tag{A.10}$$

and

$$B = -1. \tag{A.11}$$

## Appendix B. Assessing the deviatoricity of tensor quantities in the Chaboche model

Any second order tensor $\mathbf{a}$ can be decomposed into two parts, namely deviatoric and hydrostatic part:

$$\boldsymbol{a} = \boldsymbol{a}^{\text{Dev}} + \boldsymbol{a}^{\text{Hyd}} \tag{B.1}$$

with the definitions presented in equations (A.5) and (A.6). One of the properties of this decomposition is that $\mathbf{a}$ cannot be decomposed further in this sense. To clarify this property, we should decompose $\mathbf{a}^{\text{Dev}}$ and $\mathbf{a}^{\text{Hyd}}$ in the same way as in the decomposition of $\mathbf{a}$. For the deviatoric part,

$$\boldsymbol{a}^{\text{Dev}} = \left(\boldsymbol{a}^{\text{Dev}}\right)^{\text{Dev}} + \left(\boldsymbol{a}^{\text{Dev}}\right)^{\text{Hyd}} \tag{B.2}$$

where

$$\left(a^{\text{Dev}}\right)_{ij}^{\text{Hyd}} = \frac{1}{3}a_{kk}^{\text{Dev}}\delta_{ij} = \frac{1}{3}\left(a_{kk} - \frac{1}{3}a_{ll}\delta_{kk}\right)\delta_{ij} = \frac{1}{3}\left(a_{kk} - \frac{1}{3}a_{ll}\cdot 3\right)\delta_{ij} = \frac{1}{3}(a_{kk} - a_{ll})\delta_{ij} = 0$$

which is written in the compact form as

$$\left(\boldsymbol{a}^{\text{Dev}}\right)^{\text{Hyd}} = \mathbf{0}, \tag{B.3}$$

and thus

$$\left(\boldsymbol{a}^{\text{Dev}}\right)^{\text{Dev}} = \boldsymbol{a}^{\text{Dev}} - \left(\boldsymbol{a}^{\text{Dev}}\right)^{\text{Hyd}} = \boldsymbol{a}^{\text{Dev}}. \tag{B.4}$$

And, for the hydrostatic part,

$$\boldsymbol{a}^{\text{Hyd}} = \left(\boldsymbol{a}^{\text{Hyd}}\right)^{\text{Dev}} + \left(\boldsymbol{a}^{\text{Hyd}}\right)^{\text{Hyd}} \tag{B.5}$$

where

$$\left(a^{\text{Hyd}}\right)_{ij}^{\text{Hyd}} = \frac{1}{3}a_{kk}^{\text{Hyd}}\delta_{ij} = \frac{1}{3}\left(\frac{1}{3}a_{ll}\delta_{kk}\right)\delta_{ij} = \frac{1}{3}\left(\frac{1}{3}a_{ll}\cdot 3\right)\delta_{ij} = \frac{1}{3}(a_{ll})\delta_{ij} = a_{ij}^{\text{Hyd}}$$

which, again, is written in a compact form as

$$\left(\boldsymbol{a}^{\mathrm{Hyd}}\right)^{\mathrm{Hyd}} = \boldsymbol{a}^{\mathrm{Hyd}}, \tag{B.6}$$

and thus

$$\left(\boldsymbol{a}^{\mathrm{Hyd}}\right)^{\mathrm{Dev}} = \boldsymbol{a}^{\mathrm{Hyd}} - \left(\boldsymbol{a}^{\mathrm{Hyd}}\right)^{\mathrm{Hyd}} = \boldsymbol{0}. \tag{B.7}$$

Therefore, the single-step decomposition of a second order tensor **a** is proved by substituting equations (B.3) and (B.4) into (B.2) as well as equations (B.6) and (B.7) into (B.5).

The deviatoricity of a second order tensor $\boldsymbol{a}$ is defined as $\boldsymbol{a} = \mathbf{a}^{\mathrm{Dev}}$ or $\boldsymbol{a}^{\mathrm{Hyd}} = \boldsymbol{0}$. In other words, **a** is deviatoric if and only if

$$\mathrm{tr}_a = \mathrm{tr}(\boldsymbol{a}) := a_{kk} = 0 \tag{B.8}$$

where $\mathrm{tr}_a = \mathrm{tr}(\boldsymbol{a})$ is the trace of **a**. Because the trace of a is a linear combination of components of **a**,

$$\frac{\mathrm{dtr}_a}{\mathrm{d}t} = \mathrm{tr}_{\frac{\mathrm{d}a}{\mathrm{d}t}} \tag{B.9}$$

In addition, it is worth noting that $\mathrm{tr}_{a(t)} = 0$ implies $\mathrm{tr}_{\dot{a}(t)} = 0$ while $\mathrm{tr}_{\dot{a}(t)} = 0$ implies $\mathrm{tr}_{a(t)} = c_a$ where $c_a$ is a constant scalar. We will use these properties in the proof of deviatoricity of the internal force and deformation tensor.

Consider the equation of internal deformation rate (17) and substitute equation (14) and the equation of internal deformation flow direction (A.10) in it:

$$\dot{\boldsymbol{\beta}} = \dot{\lambda}\left(\sqrt{\frac{3}{2}}\ \frac{\boldsymbol{\alpha}^{\mathrm{Dev}}}{\sqrt{\boldsymbol{\alpha}^{\mathrm{Dev}} : \boldsymbol{\alpha}^{\mathrm{Dev}}}} - k_2\boldsymbol{\beta}\right) \tag{B.10}$$

then take the trace of both sides of equation:

$$\mathrm{tr}(\dot{\boldsymbol{\beta}}) = \dot{\lambda}\left(\sqrt{\frac{3}{2}}\ \frac{\mathrm{tr}(\boldsymbol{\alpha}^{\mathrm{Dev}})}{\sqrt{\boldsymbol{\alpha}^{\mathrm{Dev}} : \boldsymbol{\alpha}^{\mathrm{Dev}}}} - k_2\mathrm{tr}(\boldsymbol{\beta})\right) \tag{B.11}$$

By using the properties (B.3) and (B.9), we obtain

$$\frac{\mathrm{dtr}_\beta}{\mathrm{d}t} = \dot{\lambda}\left(-k_2\mathrm{tr}_\beta\right) \tag{B.12}$$

and, by solving this ordinary differential equation, $\mathrm{tr}_\beta$ will be

$$\mathrm{tr}_\beta = a\,\exp(-k_2\lambda) \tag{B.13}$$

where $a$ is a constant which, for example, should be determined according to an initial condition. The conventional condition of a mechanical plasticity problem is that plastic strain and all other internal deformations and forces are zero quantities for the virgin state of a material (i.e. when $\lambda$ is zero). Hence, this condition leads to $a = 0$ in equation (B.13), which means that $\mathrm{tr}_\beta$ is zero regardless of the plastic state of the material (i.e. regardless of magnitude of $\lambda$). Thus, β and consequently **χ** are deviatoric quantities in the employed equations of free energy and plastic flow potential.

Now, consider the equation of plastic strain rate in a 3D spatial space (16) and substitute the equation of plastic flow direction (A.9) in it:

$$\dot{\boldsymbol{\varepsilon}}^{\mathrm{p}} = \dot{\lambda}\left(\sqrt{\frac{3}{2}}\ \frac{\boldsymbol{\alpha}^{\mathrm{Dev}}}{\sqrt{\boldsymbol{\alpha}^{\mathrm{Dev}} : \boldsymbol{\alpha}^{\mathrm{Dev}}}}\right) \tag{B.14}$$

Obviously, $\dot{\varepsilon}^{\mathrm{p}}$ is deviatoric because of existence of the only tensor $\boldsymbol{\alpha}^{\mathrm{Dev}}$ in the right hand-side of (B.14). Thus, according to the mentioned plasticity condition of the virgin state of a material, $\varepsilon^{\mathrm{p}}$ will also be deviatoric. However, in a 2D plane strain or stress condition, we should use $\widetilde{\varepsilon^{\mathrm{p}}} = \mathsf{L}(\varepsilon^{\mathrm{p}})$ (instead of $\varepsilon^{\mathrm{p}}$) whose trace is not zero in general:

$$\mathrm{tr}\left(\widetilde{\boldsymbol{\varepsilon}^{\mathrm{p}}}\right) = \mathrm{tr}(\boldsymbol{L}(\boldsymbol{\varepsilon}^{\mathrm{p}})) = (1 + \varpi)(\varepsilon_{xx}^{\mathrm{p}} + \varepsilon_{yy}^{\mathrm{p}}). \tag{B.15}$$

Thus, $\widetilde{\varepsilon^{\mathrm{p}}}$ is not necessarily deviatoric in the plastic strain or stress condition.

## References

[1] J. Scully, The electrochemical parameters of stress-corrosion cracking, Corros. Sci. 8 (7) (1968) 513–IN18, https://doi.org/10.1016/S0010-938X(68)80006-X.

[2] J.C. Scully, THE THEORY OF STRESS CORROSION CRACKING IN ALLOYS, Anti-Corros. Methods Mater. 19 (9) (1972) 5–10, https://doi.org/10.1108/eb006879.

[3] J.C. Scully, Stress corrosion crack propagation: a constant charge criterion, Corros. Sci. 15 (4) (1975) 207–224, https://doi.org/10.1016/S0010-938X(75)80017-5.

[4] A. Turnbull, Modelling of environment assisted cracking, Corros. Sci. 34 (6) (1993) 921–960, https://doi.org/10.1016/0010-938X(93)90072-O.

[5] K. Sieradzki, R. Newman, Stress-corrosion cracking, J. Phys. Chem. Solids 48 (11) (1987) 1101–1113, https://doi.org/10.1016/0022-3697(87)90120-X.

[6] A. Turnbull, Stress Corrosion Cracking: Mechanisms, in: K.H.J. Buschow, R. W. Cahn, M.C. Flemings, B. Ilschner, E.J. Kramer, S. Mahajan, P.B.T. Veyssière (Eds.), Encyclopedia Encyclopedia of materials: science and technology, Elsevier, Oxford, 2001, pp. 8886–8891, https://doi.org/10.1016/B0-08-043152-6/01598-9 (pp).

[7] E.M. Gutman, Mechanochemistry of solid surfaces, World Scientific, Singapore, 1994.

[8] E.M. Gutman, Mechanochemistry of Materials, Cambridge International Science Pub., Cambridge, 1998.

[9] R. Dekker, F.P. derMeer, J. Maljaars, L.J. Sluys, A level set model for stress-dependent corrosion pit propagation, Int. J. Numer. Methods Eng. 122 (8) (2021) 2057–2074, https://doi.org/10.1002/nme.6614.

[10] J.S. Newman, K.E. Thomas-Alyea. Electrochemical Systems, Third ed., John Wiley,, Hoboken, N. J., 2004.

[11] J.L. Chaboche, Constitutive equations for cyclic plasticity and cyclic viscoplasticity, Int. J. Plast. 5 (3) (1989) 247–302, https://doi.org/10.1016/0749-6419(89)90015-6.

[12] R.W. Ogden, Non-linear elastic deformations, E. Horwood, Chichester, 1984.

[13] G.T. Houlsby, A.M. Puzrin, Principles of Hyperplasticity, Springer, London, 2007, https://doi.org/10.1007/978-1-84628-240-9.

[14] Y. Jiang, P. Kurath, Characteristics of the Armstrong-Frederick type plasticity models, Int. J. Plast. 12 (3) (1996) 387–415, https://doi.org/10.1016/S0749-6419(96)00013-7.

[15] J.L. Chaboche, On some modifications of kinematic hardening to improve the description of ratchetting effects, Int. J. Plast. 7 (7) (1991) 661–678, https://doi.org/10.1016/0749-6419(91)90050-9.

[16] H. Dai, S. Shi, C. Guo, X. Chen, Pits formation and stress corrosion cracking behavior of Q345R in hydrofluoric acid, Corros. Sci. 166 (2020), 108443, https://doi.org/10.1016/j.corsci.2020.108443.

[17] C. Cui, R. Ma, E. Martínez-Pañeda, A phase field formulation for dissolution-driven stress corrosion cracking, J. Mech. Phys. Solids 147 (2021), 104254, https://doi.org/10.1016/j.jmps.2020.104254.

[18] J.C. Scully, The interaction of strain-rate and repassivation rate in stress corrosion crack propagation, Corros. Sci. 20 (8) (1980) 997–1016, https://doi.org/10.1016/0010-938X(80)90080-3.